Highly Selective Electroreduction of Carbon Dioxide using Defect-driven Catalysis

Tania Akter, Caden M. Kuster,[†] Quinn A. Padovan,[†] Samuel O. Odoh,*
and Christopher J. Barile*

Department of Chemistry, University of Nevada, Reno, Reno, NV 89557, USA

[†]These authors contributed equally to this work.

*E-mail: sodoh@unr.edu, E-mail: cbarile@unr.edu

Keywords: CO_2 reduction, electrocatalyst, methanol, self-assembled monolayers, thiols, electrolyzer

Abstract

The production of methanol from the electrochemical reduction of CO_2 is a promising method of mitigating climate change while simultaneously producing a useful liquid fuel. In this study, we design self-assembled monolayers (SAMs) of thiols on metal and metal oxide electrodes that operate via cooperative catalysis between the thiolated surface sites and exposed electrode defect sites. This defect-driven mechanism enables the fabrication of SAM-modified ZnO electrodes that yield methanol with an extraordinarily high Faradaic efficiency of up to 92%. To understand the origin of this high selectivity, we study the effect of the chain length of the alkanethiols, different tail functional groups, and applied voltages on catalyst performance. These results combined with density functional theory calculations give a detailed atomic-level understanding of catalyst operation. Furthermore, the SAM linkage tolerates CO_2 reduction conditions, and the catalyst's excellent selectivity for methanol remains high after 10 hr of continuous conversion. Taken together, these findings with SAM-based electrodes convey a new and facile design strategy for the creation of highly selective CO_2 reduction electrocatalysts.

1. Introduction

The electrochemical reduction of carbon dioxide (CO_2) to value-added chemicals and fuels is a promising method of mitigating climate change.[1] A variety of products including CO, formate, methanol, ethanol, ethylene, ethane, and propanol can be produced from CO_2 reduction.[2] In general, developing catalysts with high selectivity for one of these products is a long standing challenge hindering the development of practical CO_2 electrolyzers,[3] especially given that the durability, current density,[4,5] operating overpotential,[6,7] and cost of the catalyst must be also be optimized.[3-6,8-12]

Methanol, which is generated via the six-electron reduction of CO_2, is one of the more desirable CO_2 reduction products due to its high energy density and its use in methanol fuel cells.[12-15] Catalysts based on Cu and Ag combined with other metal oxides, polymers, or alloys have been reported to facilitate the conversion of CO_2 to methanol with a wide range of Faradaic efficiencies.[16-20] In addition, various noble and non-noble metal complexes have been reported as catalysts or co-catalysts for the electrochemical synthesis of methanol.[20-25] Additionally, bimetallic composites such as Ru/Ti oxide and MoS_2/Bi_2S_3 have also been identified as catalysts for methanol production.[3,26-28] Non-noble metals such as Zn, Cu, and their alloys have also been studied for electrochemical conversion of CO_2 to methanol.[23,29,30] For example, in one study, Zn dendrites produced via pulsed electrodeposition on Ag yielded catalysts with 10.5% Faradaic efficiency for methanol.[20] Despite many efforts to convert CO_2 to methanol, achieving high Faradaic efficiency, current density, and durability simultaneously remains a challenge.[19,20,22,31] To date, only a few catalysts have been able to reach relatively high current density and selectivity (Supplementary Table 1), and the design principles that give rise to a high Faradaic

efficiency are unclear. Therefore, designing efficient catalysts to enhance activity and Faradaic efficiency is both scientifically and practically important.

Self-assembled monolayers (SAMs) of thiols have been widely studied for a variety of electrochemical applications such as catalysis and chemical sensing.[32-37] Thiol-based SAMs can exhibit excellent stability in aqueous electrolyte systems,[36-39] which makes them intriguing platforms for CO_2 reduction electrocatalysis. Previously, thiol SAMs containing pyridine moieties on Au and Pt were studied for the electrochemical reduction of CO_2 to methanol at low overpotential and low pH, but the Faradaic efficiencies for methanol production are low.[40,41]

Looking more broadly beyond CO_2 reduction, the majority of SAMs used for electrocatalysis have been performed on noble metal surfaces such as Pt, Au, and Ag, metals that by themselves are not generally used in CO_2 electrocatalysts for highly reduced products such as methanol.[31,33,37,41-43] We therefore wondered about the selectivity of thiol SAMs for CO_2 reduction on more catalytically active metal and metal oxide surfaces such as Cu, Zn, and ZnO.

In this manuscript, we describe how investigations of SAMs fabricated on these more catalytically active electrodes led us to develop thiol SAMs on ZnO electrodes that exhibit remarkably high selectivity for methanol with up to 92% Faradaic efficiency. We systematically study the role of the physicochemical properties of the SAMs on catalyst selectivity. These experiments combined with density functional theory (DFT) calculations enable us to propose a mechanistic rationale for this high selectivity, which involves the co-catalysis of thiol-modified surface sites and unmodified surface sites exposed due to SAM defects. This defect-driven catalysis represents an exciting, alternate paradigm for the fabrication of selective CO_2 reduction electrocatalysts.

2. Experimental details

2.1. Materials

Zn, Cu, Ti, and Ni foils were purchased from Belmont Metals, Inc. while Ag foil was purchased from Rio Grande, Inc. Zinc nitrate ($Zn(NO_3)_2$, 99%), potassium chloride (KCl, 99%), sodium bicarbonate ($NaHCO_3$), and acetonitrile were obtained from Oakwood Chemical, Inc. 3-mercaptopropanoic acid (98%), 3 amino-1-propanethiol (99%), 3-mercapto-1-propane sulfonate (99%), (3-mercaptopropyl) trimethoxysilane, (95%), and 3-mercato-1-propanol (99%) were purchased from Sigma Aldrich. 1-propanethiol (99%), 1-butanethiol (99%), 1-hexanethiol ($C_6H_{14}S$, 99%), 1-octanethiol (99%), and 1-decanethiol (99%) were purchased from Oakwood Chemical, Inc. 3,3,3-trifluoro-1-propanethiol (99%) was purchased from Fischer Scientific, Inc.

2.2. Electrode Preparation

Metal foils were polished using 1500-grit sandpaper. Then, they were rinsed with deionized water, subjected to sonication for 25-30 s, and rinsed thoroughly with water. To electrodeposit ZnO onto Zn foil, an aqueous solution of $Zn(NO_3)_2$ (50 mM) and KCl (100 mM) was utilized in a three-electrode cell by applying -1.2 V vs. Ag/AgCl for 10 min (Fig. S1). SAMs were deposited on all metal foils, including the ZnO deposited on Zn, using various thiols, and the presence of S on the SAM is confirmed by SEM (Fig. S2) experiment. For SAM deposition, thiol solutions in ethanol at a concentration of 10 mM were used except for the amino, sulfonate, and trimethoxysilane SAMs in which water was used because these molecules are not soluble in ethanol at 10 mM. The surfaces were then soaked for 12-14 hr to form the SAMs. Afterwards, the surfaces were rinsed with ethanol, followed by ample amounts of water.

ZnO nanoparticle electrodes were prepared using ZnO nanoparticles (30-80 nm in diameter, Jiangsu Xfnano Materials Tech.) and carbon paper (AvCarb GDS3260). Initially, ZnO nanoparticles (10 wt. %) were mixed with ethanol and sonicated for 30 min. This dispersion was

drop cast onto the carbon paper and dried under ambient air. The surface was then modified with a SAM of C_3SH, using the method previously mentioned, followed by rinsing with ethanol and water.

2.3. Electrochemical Measurements

All electrochemical measurements were conducted using a VSP-300 Biologic Potentiostat. Electrochemical data were measured against a Ag/AgCl reference electrode, and then converted to the reversible hydrogen electrode (RHE) scale using V (vs. RHE) = (V measured vs. Ag/AgCl) + 0.21 + 0.059*6.8, where 6.8 is the pH of the CO_2-sparged 0.1 M $NaHCO_3$ electrolyte. All values mentioned in this manuscript are reported versus RHE. For the $K_3Fe(CN)_6$ blocking experiment CVs, the geometric area of the working electrode was 0.22 cm^2, and a Pt wire was used as the counter electrode. Chronoamperometry experiments were conducted after the electrodes were immersed in the electrolyte for 1 hr.

2.4. Product Determination

For product determination, three-electrode chronoamperometry experiments with a geometric working electrode area of 5.0 cm^2 were performed. The geometric areas of the working electrodes were used to report current densities. Prior to each experiment, the 0.1 M $NaHCO_3$ buffer solution was sparged with CO_2 gas for at least 30 min. A two-compartment cell with a Nafion 117 membrane (Fuel Cell Store, Inc.) separator was used when ascertaining liquid and solid products. In this setup, the graphite counter electrode was placed in one compartment, while the working and reference electrodes were separated from it by the Nafion membrane (Fig. S3).

A custom-designed electrochemical cell was used for determination of gaseous products (Fig. S4). The solution volume was 2.5 mL for gaseous products and 20 mL for liquid products

with continuous CO_2 sparging during chronoamperometry at a rate of 5 cm^3 min^{-1}. To detect gaseous products, this flow rate was used to ensure that the products were swept away from the counter electrode before oxidation occurred. This interpretation is confirmed by careful experiments on known literature catalysts performed previously.[44-51] A SRI 8610C gas chromatograph equipped with a flame ionization detector and a methanizer was used to quantify gaseous products. Liquid products were analyzed using an Agilent 7890A gas chromatograph coupled to a 5975C quadrupole mass spectrometer (GC-MS). To determine liquid product concentration, an equal volume of acetonitrile was added to the electrolyte after chronoamperometry, and the mixture was stored overnight at -15°C. During this process, two separate layers formed, with the top organic layer separated and dried with anhydrous Na_2SO_4 before conducting GC-MS analysis. The efficiency of this extraction protocol was quantified using standards and accounted for when calculating Faradaic efficiency. The validity of this GC-MS method for quantifying methanol concentration was corroborated by independent ^1H NMR experiments (Fig. S5). For solid product analysis, the bottom aqueous layer was evaporated under reduced pressure, and sodium formate and other electrolyte residues were dissolved in D_2O for ^1H NMR analysis. ^1H NMR spectroscopy was conducted with a Varian 400 MHz NMR Spectrometer using DMF as an internal standard. All experiments were replicated, and error bars presented represent the standard deviation among the multiple trials. The detection limits for gases, liquid products, and formate are 1 ppm, 85 μM, and 11 μM, respectively. Faradaic efficiencies were calculated using the formula below:

Faradaic efficiency = nFzQ * 100%

where n is the number of moles from the generated product, F is Faraday's constant, z is the number of electrons transferred per molecule of the product, and Q is the total charge that is passed during CO_2 reduction.

2.5. Material Characterization

We obtained scanning electron microscopy (SEM) images and energy-dispersive X-ray (EDS) analysis using a JEOL JSN-7100F field emission SEM at an acceleration voltage of 15 kV. X-ray photoelectron spectroscopy (XPS) was performed using a Thermo Fischer Scientific Nexsa G2 Surface Analysis System using a monochromatic Al X-ray source and a spot size of 400 μm. The energies of the spectra were calibrated against the C 1s peak of adventitious carbon at 248.6 eV.

2.6. Periodic DFT Calculations

Periodic DFT computations within the projector-augmented wave (PAW) formalism were performed with the Vienna ab initio package (VASP)[52-55] while employing the PBE[56] functional with the D3BJ[57,58] damping correction and a plane wave basis with an energy cutoff of 500 eV. Starting from the wurtzite structure of ZnO, we modelled the non-polar $(10\bar{1}0)$ surface as a five-layer slab of 120 atoms, with a vacuum spacing of 25 Å between periodic images to avoid spurious interactions in the Z-axis. On bare ZnO$(10\bar{1}0)$, we considered stepwise reduction of CO_2 to the *COH and *CHO intermediates via *COOH. To describe the impact of surface functionalization on CO_2 reduction, we added a propanethiolate ligand ($CH_3CH_2CH_2S$) to the top surface of the slab, labelled as C_3SH-ZnO$(10\bar{1}0)$. The presence of this thiolate yields new binding modes for CO_2 and the CO intermediates. We fully relaxed the reaction intermediates, thiolates, as well as the top two layers of the slab until the maximum force on each atom was less than 0.01 eV $Å^{-1}$. The bottom three layers were always kept fixed. Dipole moment corrections to

the total energy were employed in the Z-direction, and the total energy convergence criterion was set at 1×10^{-5} eV. The Brillouin zone was sampled with a 2×2×1 Monkhorst-Pack k-point mesh for all calculations. In all calculations, we assumed spin polarization (ISPIN = 2) and accounted for solvation effects, using the VASPsol[59,60] module with water as the solvent. To compute the Gibbs free energies of adsorbed species, we incorporate zero-point energy (ZPE) and entropy corrections. ZPE values are obtained from the frequencies of all vibrations of the surface adsorbates on the slab. To compute these frequencies, all atoms of the ZnO slab were held fixed. Vibrational contribution to the entropy of the molecules and the adsorbed species are calculated in the usual way from these frequencies using 298.15 K as the temperature and a pressure of 1 atm. In the solid state, volume changes are typically very small, and therefore the small difference between enthalpy and energy is not considered. These analyses were performed with VASPKIT.[61]

3. Results and Discussion

3.1. Rationale for Designing SAM-modified Electrodes for Selective CO_2 Reduction

Our laboratory previously demonstrated that fluoropolymer-modified metal electrodes can be used to elicit CO_2 reduction with high selectivity.[44-50] In particular, we found that Cu electrodes modified with an overlayer of Nafion produce CH_4 with high Faradaic efficiencies up to 88% (Fig. 1A) during the electrochemical reduction of CO_2.[44] This high selectivity is attributed to the stabilization of a metal-bound CO intermediate that interacts with the sulfonate groups of the Nafion layer. By modulating the hydrophobicity of the fluoropolymer overlayer and the underlying metal electrode used, we were able to design polymer-modified electrodes that exhibit high Faradaic efficiencies for several other CO_2 reduction products including ethylene and ethanol.[45]

Although electrodes covered with fluoropolymers such as Nafion are effective in facilitating selective CO_2 conversion, the polymer layers used are tens of microns thick, which makes the electrodes expensive to fabricate and causes them to exhibit poor durability due to delamination from the electrode surface during catalysis.[44-46,51,62] As such, we were inspired to replace the physiosorbed polymer overlayers with chemisorbed thiol-based SAMs that should exhibit increased durability. Furthermore, the chemical structure of the SAMs can be tuned to mimic the chemical properties of the polymer layers and elucidate the chemical origins of catalyst selectivity and reactivity.[63]

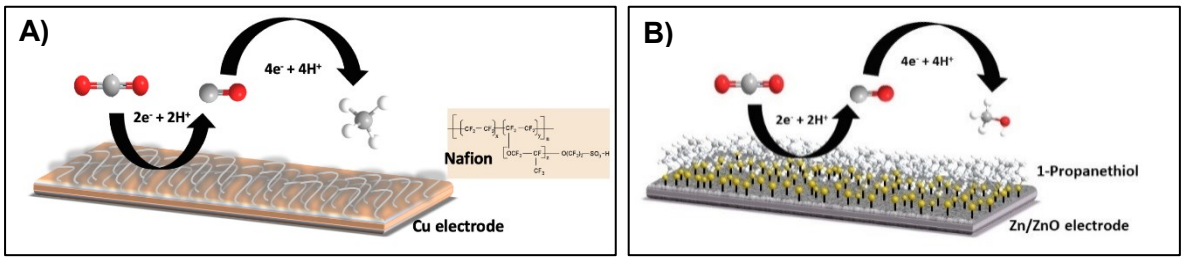

Figure 1. Schematic of a Nafion-polymer modified Cu electrode for the selective reduction of CO_2 to CH_4 (A) and a ZnO electrode modified with a SAM of 1-propanethiol (C_3SH) for the selective reduction of CO_2 to methanol (B).

We discovered that SAMs of 1-propanethiol (C_3SH) on ZnO (Fig. 1B) yield electrocatalysts that convert CO_2 to methanol with a Faradaic efficiency as high as 92%. DFT calculations and surface characterization experiments suggest that the high selectivity for methanol production results from an interplay between the thiol-modified ZnO sites on the electrode and unmodified ZnO defect sites present on the surface.

3.2. SAM-Modified ZnO Electrodes for Selective Methanol Production

ZnO is a well-known CO_2 reduction electrocatalyst, and it can produce over 90% Faradaic efficiency for CO, which is a crucial intermediate in the generation of more highly reduced products.[64] Because there is precedence for forming thiol SAMs on ZnO surfaces,[64,65]

we were inspired to use SAMs on ZnO electrodes for CO_2 reduction to impart molecular level control over reactivity. Remarkably, a SAM of C_3SH on a ZnO electrode yields 88% Faradaic efficiency for methanol after 1 hour of chronoamperometry at -1.4 V vs. RHE (Fig. S6) with only minor amounts of HCOOH, ethanol, and H_2 side products (Fig. 2A, rightmost set of bars). Additional experiments indicate that the combination of ZnO and C_3SH is needed to produce methanol. Unmodified Zn and ZnO electrodes produce predominantly CO without any methanol as is known in the literature,[64,66] and C_3SH deposited on Zn also does not generate any methanol. Additionally, CO_2 reduction performed on C_3SH SAMs on other metal electrodes including Ni, Ag, Cu, and Ti (Fig. S7) do not yield any methanol (Fig. S8). Taken together, these results demonstrate that C_3SH and ZnO function synergistically to enable selective methanol production.

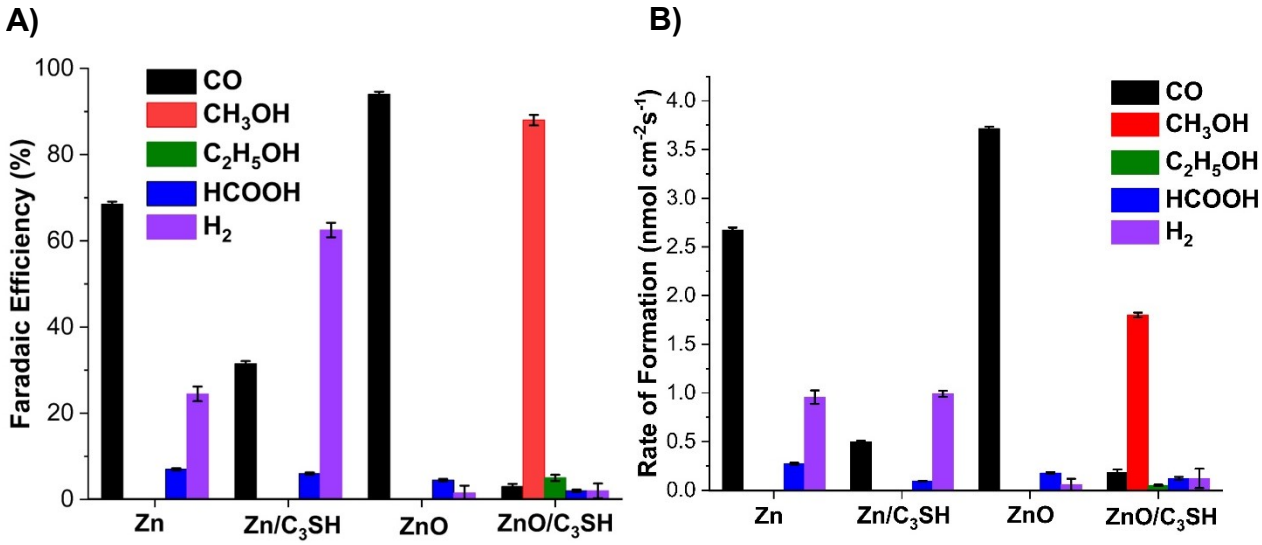

Figure 2. Faradaic efficiencies (A) and rates of formation (B) for CO (black), methanol (red), C_2H_5OH (green), HCOOH (blue), and H_2 (yellow) after 1 hr of CO_2 reduction at -1.4 V vs. RHE using electrodes consisting of unmodified Zn metal, Zn modified with a C_3SH SAM, unmodified ZnO, and ZnO modified with a C_3SH SAM.

After establishing that a SAM of C_3SH on the ZnO electrode facilitates methanol generation, we investigated the effect of different voltages on catalyst selectivity (Fig. S9). At -0.6 V vs RHE, H_2 is the primary product with minor selectivity for CO, methanol, and

formate (Fig. S10). At -0.9 V vs. RHE, the selectivity of methanol is maximized at 92% Faradaic efficiency, and the methanol Faradaic efficiency progressively degreases at more negative voltages. The C_3SH-modified ZnO electrode also facilitates CO reduction to methanol with a high Faradaic efficiency of 91% at -0.9 V vs. RHE (Fig. S11). This result indicates that CO is a key intermediate in the reduction of CO_2 to methanol via this catalyst.

We also tested the effect of various functional groups on ZnO SAMs with three-carbon chain lengths (Fig. 3 and Fig. S12). Interestingly, hydrophilic functional groups on the tail of the SAM including carboxylate, amino, alcohol, and sulfonate completely inhibit methanol production, while a trifluoromethyl group only partially hinders the catalyst's selectivity for methanol. These results demonstrate that hydrophobic SAMs are necessary for methanol production on ZnO electrodes.

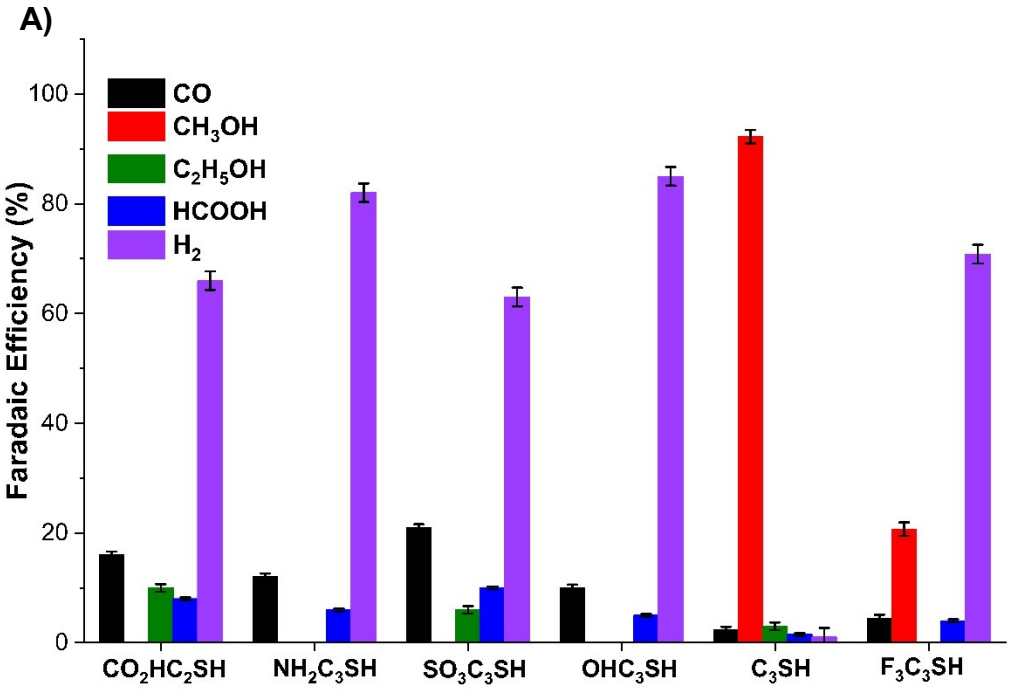

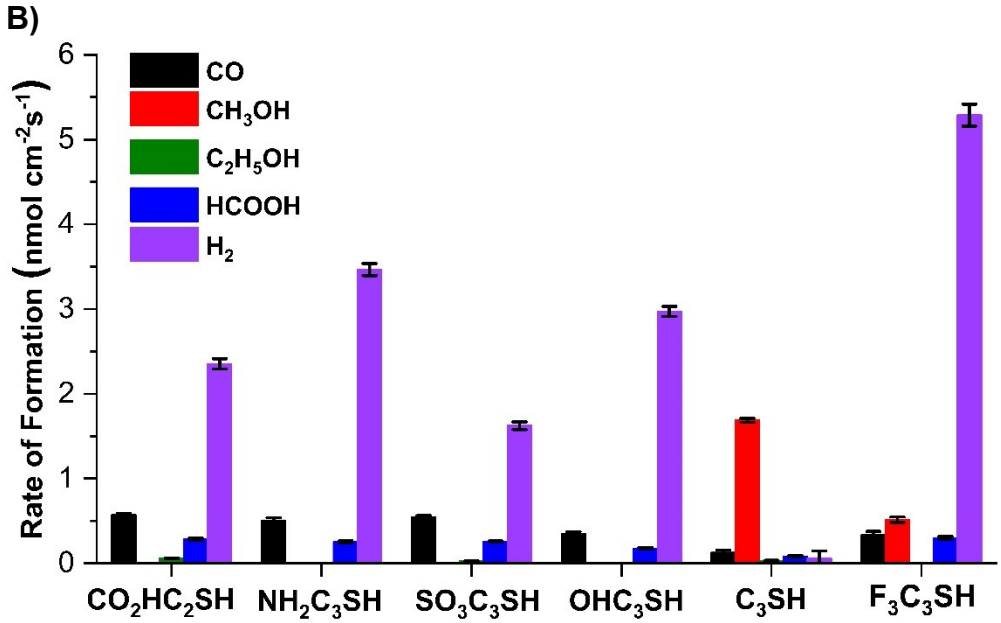

Figure 3. Faradaic efficiencies (A) and rates of formation (B) for CO (black), methanol (red), C_2H_5OH (green), HCOOH (blue), and H_2 (purple) after 1 hr of CO_2 reduction at -0.9 V vs. RHE using ZnO deposited Zn electrode fabricated by different thiol group. CO_2HC_2SH, NH_2C_3SH, SO_3C_3SH, OHC_3SH, C_3SH, and F_3C_3SH, represent 3-mercaptopropanoic acid, 3-amino-1-propanethiol, 3-mercapto-1-propane sulfonate, 3-mercapto-1-propanol, 1-propanethiol, and 3,3,3-trifluoro-1-propanethiol, respectively.

3.3. Mechanistic Interpretations: Evidence for Defect-driven Catalysis from DFT Calculations

From the results above, we demonstrate that a hydrophobic SAM on ZnO exhibits unique chemical reactivity that gives rise to the selective electroreduction of CO_2 to methanol. We therefore utilize DFT calculations to interrogate what mechanistic attributes of the C_3SH-ZnO catalyst enable methanol formation. These calculations provide Gibbs free energies of electrochemical reactions, with corrections for solvation at 0 V versus the RHE. Adsorption free energies, ΔG, for CO_2 or CO are defined by

$$\Delta G = G_{sub/gas} - E_{sub} - G_{gas}$$

where $G_{sub/gas}$ is the free energy of the substrate with bound adsorbate, E_{sub} is the total electronic energy of the substrate, and G_{gas} is the free energy of the adsorbate in the gas phase.

CO_2 binds to ZnO($10\bar{1}0$) as a tridentate carbonate, with a binding energy of 0.89 eV (Fig. 4). On a C_3SH-ZnO($10\bar{1}0$) model with one thiolate ligand, the surface-bound tridentate carbonate

mode remains the most stable binding mode, 0.93 eV, significantly more so than the thiocarbonate mode, 0.12 eV, where CO_2 is bound directly to the thiolate. Thus, the CO_2 adsorption free energy is not affected by the thiolate, at least at the considered surface coverage, and there is very little impetus for CO_2 to bind directly to the thiol. CO_2 reduction will therefore mostly commence at exposed ZnO islands on surfaces coated with C_3SH SAMS.

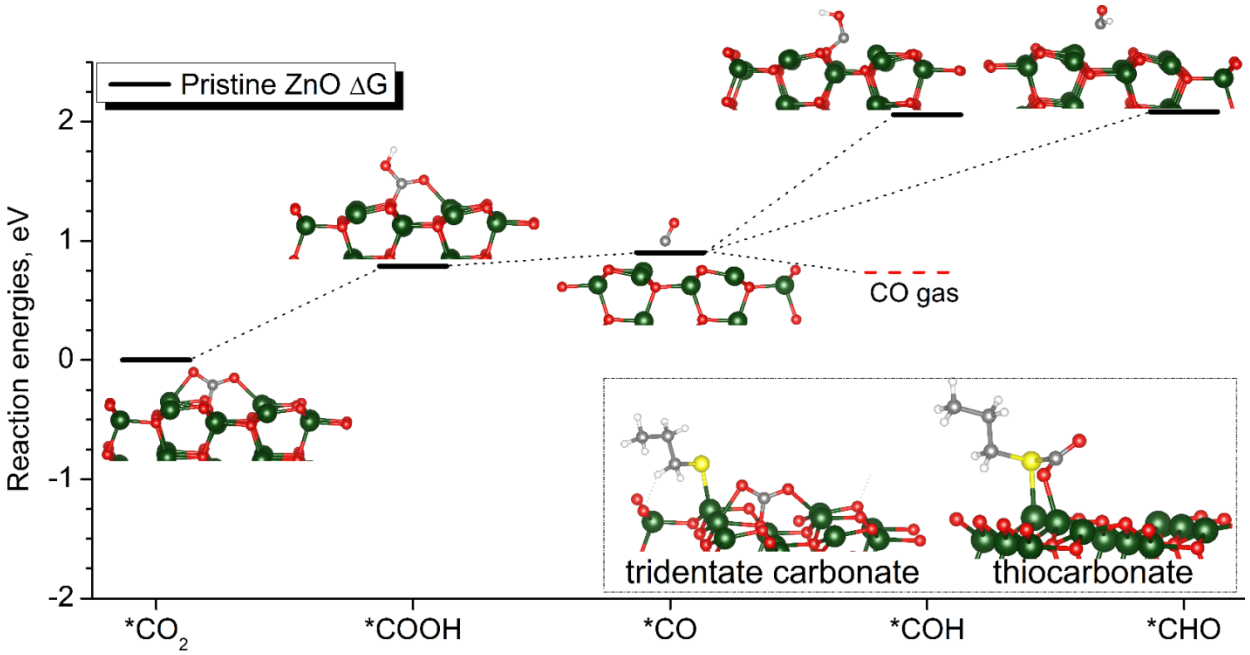

Figure 4. Energy diagram for CO_2 reduction on ZnO($10\bar{1}0$). Binding modes of CO_2 on C_3SH-ZnO($10\bar{1}0$) are shown in the inset.

Regarding CO_2 reduction, the Gibbs free energy for forming *COOH on ZnO($10\bar{1}0$) is 0.79 eV. Further reduction of *COOH to *CO and desorbed water brings the total free energy to 0.90 eV. In Fig. 5, *CO is adsorbed on ZnO($10\bar{1}0$) in a near-linear mode, through the end of the carbon, to a surface Zn atom. Further reduction of *CO to either *HCO or *COH is significantly disfavored on ZnO($10\bar{1}0$), by +1.15 eV or +1.18 eV, respectively. Interestingly, desorption of CO from the ZnO($10\bar{1}0$) surface costs +0.17 eV, far smaller than the *CO → *COH/*HCO reduction energies, and it is thus easy to rationalize why the pristine ZnO($10\bar{1}0$) surface is a CO_2 to CO reduction electrocatalyst.

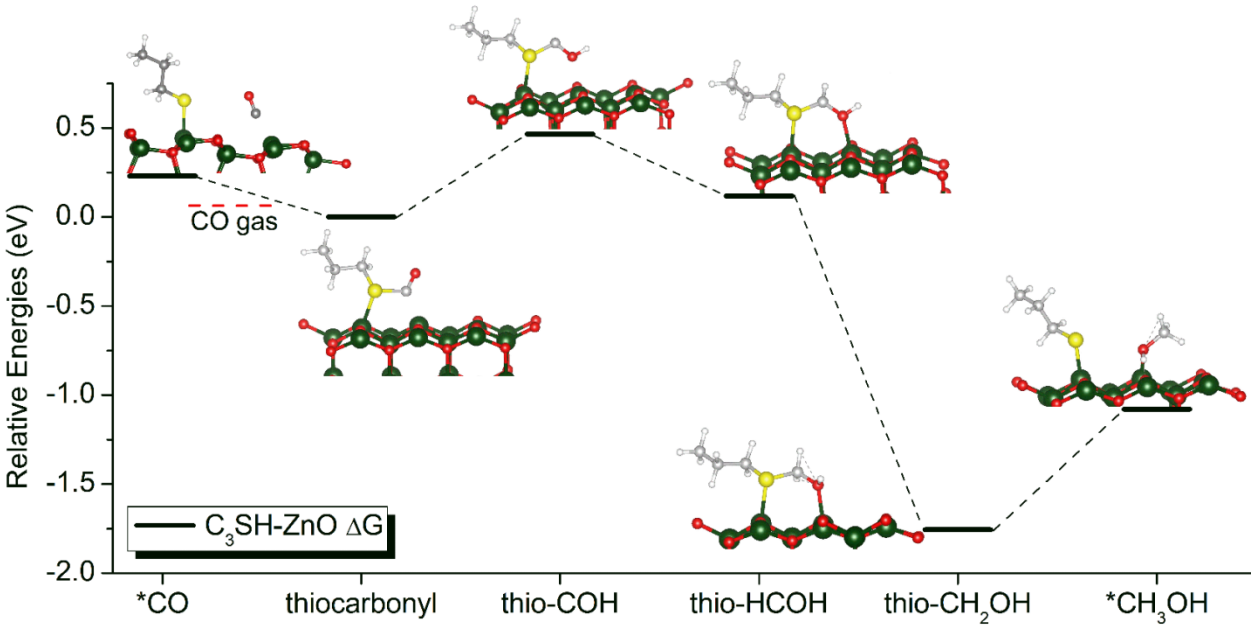

Figure 5. Energy diagram for CO reduction on the C_3SH-ZnO($10\bar{1}0$) surface.

Having established that CO_2 preferentially binds to the ZnO surface where electrochemical reduction to CO is facilitated, we consider the binding configurations of CO on C_3SH-ZnO($10\bar{1}0$). Indeed, there are two binding configurations for CO on C_3SH-ZnO($10\bar{1}0$), either, like for pristine ZnO($10\bar{1}0$), to a Zn atom, or as a thiocarbonyl, interacting with the thiolate sulfur atom (C-S distance of 1.87 Å) and also with a surface Zn atom (C-Zn distance of 2.10 Å, Fig. 5). Interestingly, the thiocarbonyl binding mode for CO on C_3SH-ZnO($10\bar{1}0$) is 0.23 eV stronger than the *CO surface-binding mode on this substrate, indicating that the thiolate ligand provides a new destination for desorbed CO previously formed on exposed ZnO($10\bar{1}0$) islands. Moreover, the thiocarbonyl is much readily reduced to thio-COH, costing only 0.47 eV. Thus, this new binding mode afforded by the thiolate allows for further reduction of CO produced on ZnO. Downstream reduction of the thio-COH to thio-HCOH and subsequently to thio-CH_2OH and finally surface-bound methanol, *CH_3OH, are energetically favored, and significantly preferred to dehydration alternatives (specifically thio-C and thio-CH) that would otherwise lead to formation of CH_4.

3.4. Further Evidence for Defect-driven Catalysis from Chain Length Studies

Given that the DFT analysis above suggests that the interplay between unmodified ZnO defect sites and C_3SH-ZnO sites facilitates methanol production, we studied the effect of different SAM chain lengths with different defect densities on catalyst selectivity. In SAMs, defect sites commonly occur, and the defects refer to the exposed, unmodified portions of the electrode. Higher chain length SAMs generally have a greater packing density due to favorable van der Waals interactions between the methylene groups, which results in a lower SAM defect density.[67,68] To confirm that this trend is true for ZnO surfaces, we conducted standard $K_3Fe(CN)_6$ blocking experiments on various alkylthiol ZnO SAMs. A cyclic voltammogram (CV) of a ZnO electrode modified with C_3SH exhibits substantially less current density than that of an unmodified ZnO electrode (Fig. 6A). This result is expected because the C_3SH SAM impedes electron transfer kinetics to the solution-phase $Fe(CN)_6^{3-}$ redox couple. However, the $Fe(CN)_6^{3-}$ redox couple is still clearly present with the C_3SH SAM. Although impeded, electron transfer from the surface to $Fe(CN)_6^{3-}$ still occurs through unmodified ZnO sites on the electrode (SAM defect sites) and via electron tunneling through the SAM. As the chain length of the SAM is increased from C3 to C10, the ratio of integrated charge passed in the $Fe(CN)_6^{3-}$ blocking CV for the SAM electrode compared to the unmodified ZnO electrode progressively decreases from 0.11 to 0.06 (Fig. S13A). Furthermore, in general, there is a progressive increase in the peak-to-peak separation with increased SAM chain length, which is diagnostic of increasingly hindered electron transfer rates (Fig. 6B). Interestingly, however, the peak-to-peak separation is larger for C3 than it is for C4, which goes against this trend and suggests that the electron transfer rate of the C3-modified SAM is slower than that of the C4-modified SAM. Laviron electron transfer rates calculated from CVs conducted at variable scan rates[69] confirm this behavior (Figs. S13B and S13C), which possibly originates from poorer packing dynamics of the C4 SAM. Lastly,

water contact angle measurements demonstrate that the longer chain length SAMs are more hydrophobic (Fig. S14 and Table S2). The $K_3Fe(CN)_6$ blocking and water contact angle measurements both provide evidence that higher chain length ZnO SAMs exhibit greater packing densities and lower defect densities.

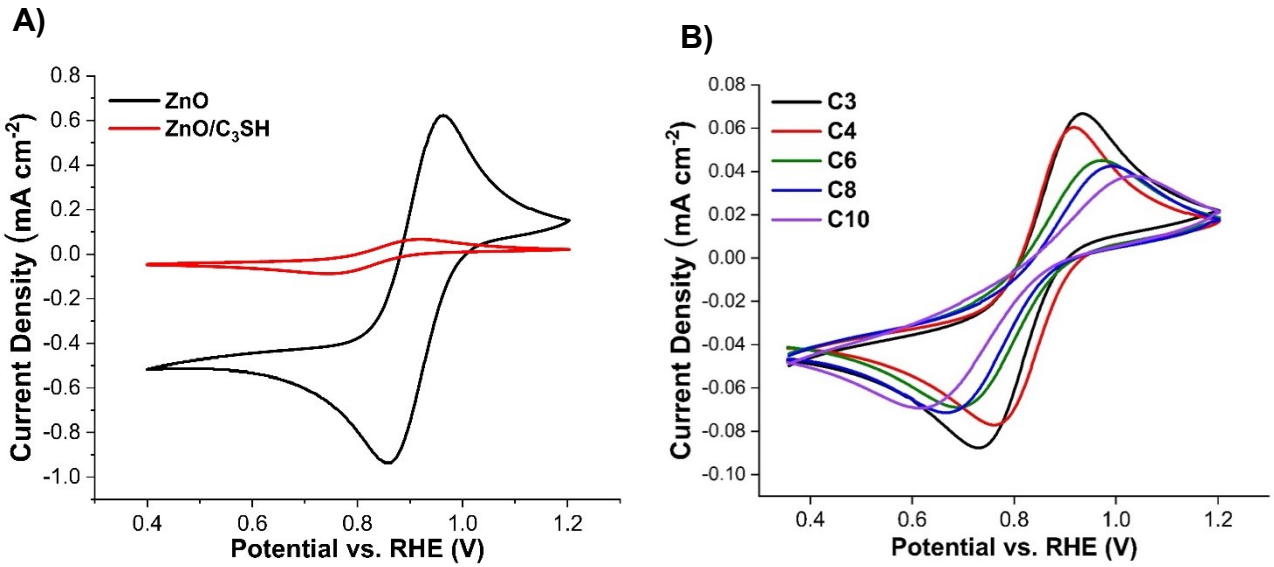

Figure 6. Cyclic voltammograms of bare ZnO (A, black) and C_3SH-modified ZnO electrodes (A, red) and ZnO modified with SAMs with different alkanethiol carbon chain lengths including C3 (B, black), C4 (B, red), C6 (B, green), C8 (B, blue), and C10 (B, purple) at 5 mV s^{-1} in 5 mM $K_3Fe(CN)_6$ with 0.1 M KCl in H_2O.

$K_3Fe(CN)_6$ blocking experiments conducted on ZnO C3 SAMs with various tail functional groups do not yield significantly different CVs because the lengths of the SAMs are all similar (Fig. S15). However, as discussed earlier, the CO_2 product distribution is very sensitive to the identity of the tail functional group (Fig. 3). The methyl and trifluoromethyl SAMs are the most hydrophobic as indicated by water contact angle measurements (Fig. S16 and Table S3), the two C3 SAMs that yield significant quantities of methanol.

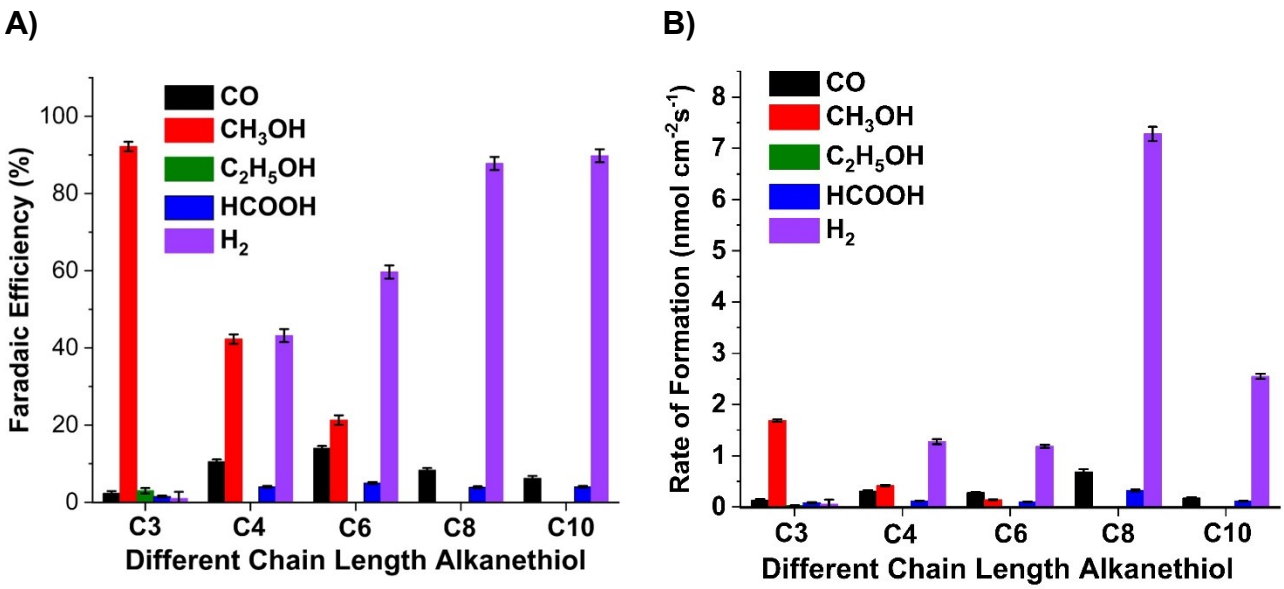

Figure 7. Faradaic efficiencies (A) and rates of formation (B) for CO (black), methanol (red), C_2H_5OH (green), HCOOH (blue), and H_2 (purple) after 1 hr of CO_2 reduction at -0.9 V vs. RHE using ZnO electrodes modified with alkanethiol SAMs containing different carbon chain lengths. Representative chronoamperometry data are presented in Figure S16.

The data in Fig. 7 (Fig. S17) demonstrate that the selectivity for methanol production decreases as the SAM chain length increases from C3 to C6, and no methanol was detected for the C8 and C10 SAMs. The C_3SH-ZnO electrode exhibits the highest Faradaic efficiency as this monolayer is the least densely packed, and thus contains the highest number of defect sites that the previously discussed DFT calculations indicate are necessary for methanol generation. Taken together, these results demonstrate that defect density and tail functional groups both affect product distribution and that defect-rich SAMs with hydrophobic tail groups are the most selective for methanol.

3.5. Practical Considerations: Catalyst Durability and Nanostructuring

After gaining mechanistic insight into the origin of methanol selectivity facilitated by the C_3SH-ZnO catalyst, we evaluated its catalytic stability through a 21-hour test at -0.9 V vs RHE. The results are impressive, showing that the catalyst is relatively stable, with the Faradaic efficiency slightly decreasing from 92% to 86% during the first 10 hours of the test before

decreasing further to 78% after 21 hours (Fig. 8). XPS experiments show that the SAM remains mostly intact after CO_2 reduction as evidenced by the S peak at 164 eV (Fig. S18), which originates from the thiol group of C_3SH. However, the intensity of the S peak relative to the Zn peaks decreases after chronoamperometry, suggesting that some C_3SH is lost from the surface during catalysis. This decrease in C_3SH surface coverage likely explains the decrease in Faradaic efficiency for methanol production witnessed over the course of 21 hours of catalysis.

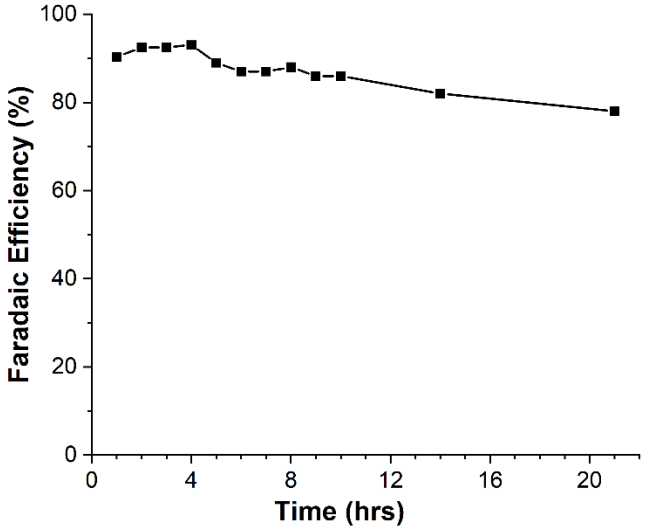

Figure 8. Faradaic efficiency for methanol production over time of a ZnO electrode modified with a C_3SH SAM using chronoamperometry at -0.9 V vs. RHE.

In addition to durability, current density is another important practical consideration for catalysts. Compared to several other reported CO_2 reduction catalysts,[44-49,70] the relatively low current densities reported thus far in this manuscript are expected because the electrodes we use are nominally flat, unlike highly porous electrodes designed to maximize current density. The behavior of SAMs on flat electrodes, however, is much simpler than highly porous electrodes, and there are fewer types of active sites on flat electrodes, which aids in mechanistic understanding and allows for more accurate DFT modeling. After elucidating the chemical

properties that give rise to high methanol Faradaic efficiencies on the flat C_3SH-ZnO catalyst, we next nanostructured the catalyst as a first step towards developing a practical catalytic system with increased current density.

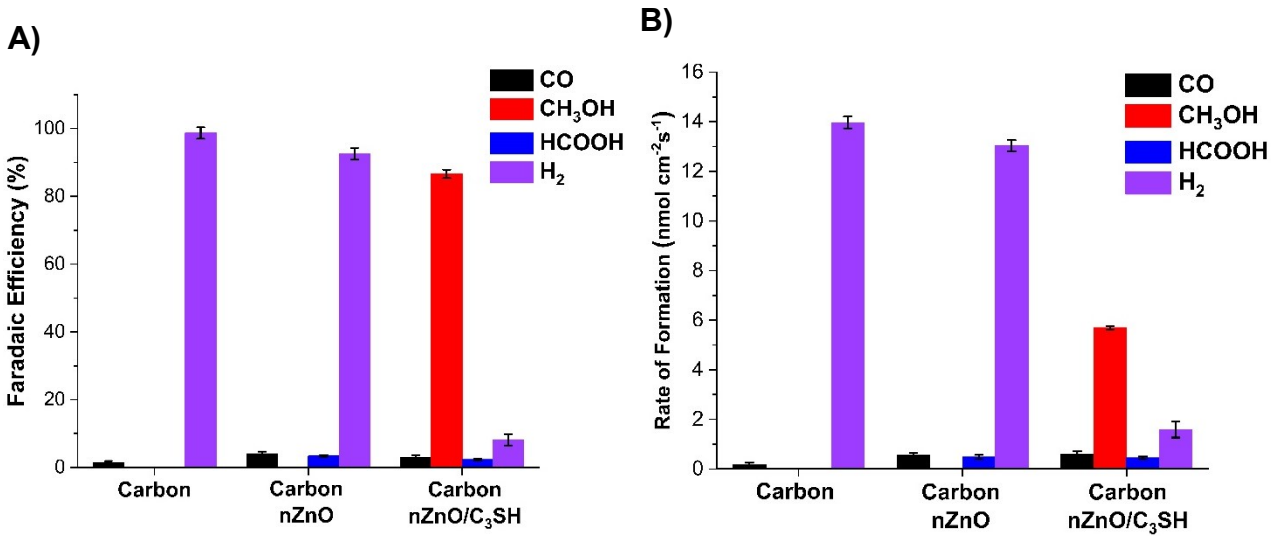

Figure 9. Faradaic efficiencies (A) and rates of formation (B) for CO (black), methanol (red), HCOOH (blue), and H_2 (purple) after 1 hr of CO_2 reduction at -0.9 V vs. RHE using carbon paper, carbon paper modified with ZnO nanoparticles, and carbon paper modified with ZnO nanoparticles with a SAM of C_3SH.

The nanostructured catalyst (nZnO/C_3SH) consists of C_3SH deposited on commercially available 30-80 nm in diameter ZnO drop cast on carbon paper. This nZnO/C_3SH catalyst retains high selectivity for methanol during CO_2 reduction with a Faradaic efficiency of 88% (Fig. 9 and Fig. S19). In a manner analogous to the flat electrodes, the nanostructured catalyst with C_3SH or without ZnO does not generate any methanol. These results indicate that the synergism between ZnO and C_3SH for methanol selectivity is maintained even when the catalyst is nanostructured in a form that is amenable for more practical CO_2 reduction devices.

4. Conclusions

In summary, we describe SAM-modified metal and metal oxide electrocatalysts that enable highly selective CO_2 conversion. This general class of catalysts enables selective production of CH_4 in the case of Cu and methanol in the case of ZnO. In particular, a SAM of

C_3SH on a ZnO electrode yields methanol at 92% Faradaic efficiency at -0.9 V vs. RHE. In contrast, ZnO electrodes without SAMs do not produce any methanol and instead predominantly generate CO. Based on systematic studies with various SAMs and DFT calculations, we propose a novel defect-driven mechanism for electrochemical CO_2 conversion that explains the high selectivity observed. In this mechanism, CO is produced at unmodified ZnO exposed as defect sites in the SAM, and the thiol moiety of C_3SH facilitates the subsequent conversion of CO to methanol. This mechanism outlines a new paradigm for the rational design of selective CO_2 conversion electrocatalysts using defect-rich SAMs as a platform for co-catalysis.

Author Contributions

C.J.B. and S.O.O. supervised the project. T.A. and C.J.B. designed the experiments. T.A., Q.A.P., and C.M.K. conducted the experiments. T.A., S.O.O., and C.J.B. wrote the paper. S.O.O. performed all computational calculations. All authors discussed the results of the manuscript and analyzed the data.

Competing Interests

T.A., Q.A. P., C.M.K., and C.J.B. have filed a provisional patent related to this work. The other authors declare no competing interests.

Supporting Information

Additional electrochemical data, ^1H NMR data, water contact angle measurements, XPS data, DFT data, and survey of other CO_2 to methanol catalysts in the literature.

Acknowledgements

T.A., Q.A.P., C.M.K., and C.J.B. acknowledge support from the National Science Foundation CAREER Award under Grant No. CHE-2046105. We acknowledge the Shared Instrumentation Laboratory in the Department of Chemistry at UNR. We also acknowledge the Mackay

Microbeam Laboratory and Dr. J. DesOrmeau at UNR for assistance with the SEM-EDS analysis.

References

1. Shi, R.; Wang, Z.; Zhao, Y.; Waterhouse, G. I. N.; Li, Z.; Zhang, B.; Sun, Z.; Xia, C.; Wang, H.; Zhang, T. Room-temperature electrochemical acetylene reduction to ethylene with high conversion and selectivity. *Nat. Catal.* **2021**, *4*, 565 - 574.
2. Gao, D.; Li, W.; Wang, H.; Wang, G.; Cai, R. Heterogeneous Catalysis for CO_2 Conversion into Chemicals and Fuels. *Trans. Tianjin Univ.* **2022**, *28*, 245-264.
3. Sun, X.; Zhu, Q.; Kang, X.; Liu, H.; Qian, Q.; Zhang, Z.; Han, B. Molybdenum–Bismuth Bimetallic Chalcogenide Nanosheets for Highly Efficient Electrocatalytic Reduction of Carbon Dioxide to Methanol. *Angew. Chem. Int. Ed.* **2016**, *55* (23), 6771-6775.
4. Barton Cole, E.; Lakkaraju, P. S.; Rampulla, D. M.; Morris, A. J.; Abelev, E.; Bocarsly, A. B. Using a One-Electron Shuttle for the Multielectron Reduction of CO_2 to Methanol: Kinetic, Mechanistic, and Structural Insights. *J. Am. Chem. Soc.* **2010**, *132* (33), 11539-11551.
5. Heyduk, A. F.; Macintosh, A. M.; Nocera, D. G. Four-Electron Photochemistry of Dirhodium Fluorophosphine Compounds. *J. Am. Chem. Soc.* **1999**, *121* (21), 5023-5032.
6. Chen, Y.; Li, C. W.; Kanan, M. W. Aqueous CO_2 Reduction at Very Low Overpotential on Oxide-Derived Au Nanoparticles. *J. Am. Chem. Soc.* **2012**, *134* (49), 19969-19972.
7. Li, C. W.; Kanan, M. W. CO_2 Reduction at Low Overpotential on Cu Electrodes Resulting from the Reduction of Thick Cu_2O Films. *J. Am. Chem. Soc.* **2012**, *134* (17), 7231-7234.

8. Lee, J. H. Q.; Lauw, S. J. L.; Webster, R. D. The electrochemical reduction of carbon dioxide (CO_2) to methanol in the presence of pyridoxine (vitamin B6). *Electrochem. Commun.* **2016**, *64*, 69-73.
9. Bagger, A.; Christensen, O.; Ivaništšev, V.; Rossmeisl, J. Catalytic CO_2/CO Reduction: Gas, Aqueous, and Aprotic Phases. *ACS Catal.* **2022**, *12* (4), 2561-2568.
10. Larrea, C.; Avilés-Moreno, J. R.; Ocón, P. Strategies to Enhance CO_2 Electrochemical Reduction from Reactive Carbon Solutions. *Molecules*, **2023**, 28 (4), 1951-1963.
11. Wen, C. F.; Zhou, M.; Liu, P. F.; Liu, Y.; Wu, X.; Mao, F.; Dai, S.; Xu, B.; Wang, X. L.; Jiang, Z.; et al. Highly Ethylene-Selective Electrocatalytic CO_2 Reduction Enabled by Isolated Cu−S Motifs in Metal–Organic Framework Based Precatalysts. *Angew. Chem. Int. Ed.* **2022**, *61* (2), e202111700.
12. Yang, H.-P.; Yue, Y.-N.; Qin, S.; Wang, H.; Lu, J.-X. Selective electrochemical reduction of CO_2 to different alcohol products by an organically doped alloy catalyst. *Green Chem.* **2016**, *18* (11), 3216-3220, 10.1039/C6GC00091F.
13. Studt, F.; Sharafutdinov, I.; Abild-Pedersen, F.; Elkjær, C. F.; Hummelshøj, J. S.; Dahl, S.; Chorkendorff, I.; Nørskov, J. K. Discovery of a Ni-Ga catalyst for carbon dioxide reduction to methanol. *Nat. Chem.* **2014**, *6* (4), 320-324.
14. Alias, M. S.; Kamarudin, S. K.; Zainoodin, A. M.; Masdar, M. S. Active direct methanol fuel cell: An overview. *Int. J. Hydrog. Energy.* **2020**, *45* (38), 19620-19641.
15. Reddy, V. J.; Hariram, N. P.; Maity, R.; Ghazali, M. F.; Kumarasamy, S. Sustainable E-Fuels: Green Hydrogen, Methanol and Ammonia for Carbon-Neutral Transportation. *World Electr. Veh. J.* **2023**, *14* (12), 349-367.
16. Yang, D.; Zhu, Q.; Chen, C.; Liu, H.; Liu, Z.; Zhao, Z.; Zhang, X.; Liu, S.; Han, B. Selective electroreduction of carbon dioxide to methanol on copper selenide nanocatalysts. *Nat. Commun.* **2019**, *10* (1), 677.
17. Albo, J.; Sáez, A.; Solla-Gullón, J.; Montiel, V.; Irabien, A. Production of methanol from CO2 electroreduction at Cu_2O and Cu_2O/ZnO-based electrodes in aqueous solution. *Appl. Catal. B: Environ.* **2015**, *176-177*, 709-717.
18. Xie, S.; Zhang, W.; Lan, X.; Lin, H. CO_2 Reduction to Methanol in the Liquid Phase: A Review. *ChemSusChem* **2020**, *13* (23), 6141-6159.

19. Ding, J.; Tang, Q.; Fu, Y.; Zhang, Y.; Hu, J.; Li, T.; Zhong, Q.; Fan, M.; Kung, H. H. Core–Shell Covalently Linked Graphitic Carbon Nitride–Melamine–Resorcinol–Formaldehyde Microsphere Polymers for Efficient Photocatalytic CO_2 Reduction to Methanol. *J. Am. Chem. Soc.* **2022**, *144* (22), 9576-9585.
20. Low, Q. H.; Loo, N. W. X.; Calle-Vallejo, F.; Yeo, B. S. Enhanced Electroreduction of Carbon Dioxide to Methanol Using Zinc Dendrites Pulse-Deposited on Silver Foam. *Angew. Chem. Int. Ed.* **2019**, *58* (8), 2256-2260.
21. Le, M.; Ren, M.; Zhang, Z.; Sprunger, P. T.; Kurtz, R. L.; Flake, J. C. Electrochemical Reduction of CO_2 to CH_3OH at Copper Oxide Surfaces. *J. Electrochem. Soc.* **2011**, *158* (5), E45.
22. Vieira, L. H.; Rasteiro, L. F.; Santana, C. S.; Catuzo, G. L.; da Silva, A. H. M.; Assaf, J. M.; Assaf, E. M. Noble Metals in Recent Developments of Heterogeneous Catalysts for CO2 Conversion Processes. *ChemCatChem* **2023**, *15* (14), e202300493.
23. Summers, D. P.; Leach, S.; Frese, K. W. The electrochemical reduction of aqueous carbon dioxide to methanol at molybdenum electrodes with low overpotentials. *J. Electroanal. Chem. Interf. Electrochem.* **1986**, *205* (1), 219-232.
24. Lu, L.; Sun, X.; Ma, J.; Yang, D.; Wu, H.; Zhang, B.; Zhang, J.; Han, B. Highly Efficient Electroreduction of CO_2 to Methanol on Palladium–Copper Bimetallic Aerogels. *Angew. Chem. Int. Ed* **2018**, *57* (43), 14149-14153.
25. Morales-Guio, C. G.; Cave, E. R.; Nitopi, S. A.; Feaster, J. T.; Wang, L.; Kuhl, K. P.; Jackson, A.; Johnson, N. C.; Abram, D. N.; Hatsukade, T.; Hahn, C.; Jaramillo, T. F. Improved CO_2 reduction activity towards C2+ alcohols on a tandem gold on copper electrocatalyst. *Nat. Catal.* **2018**, *1* (10), 764-771.
26. Malpass, G. R. P.; Motheo, A. J. Galvanostatic oxidation of formaldehyde-methanol solutions on Ti/Ru0.3Ti0.7O2 electrodes using a filter-press cell. *J. Appl. Electrochem.* **2001**, *31* (12), 1351-1357.
27. Irikura, K.; Perini, J. A. L.; Flor, J. B. S.; Frem, R. C. G.; Zanoni, M. V. B. Direct synthesis of Ru3(BTC)2 metal-organic framework on a Ti/TiO2NT platform for improved performance in the photoelectroreduction of CO_2. *J. CO_2 Utiization* **2021**, *43*, 101364.

28. Li, Z.; Ivanenko, A.; Meng, X.; Zhang, Z. Photocatalytic oxidation of methanol to formaldehyde on bismuth-based semiconductors. *J. Hazard. Mater.* **2019**, *380*, 120822.
29. Kaneco, S.; Ueno, Y.; Katsumata, H.; Suzuki, T.; Ohta, K. Electrochemical reduction of CO_2 in copper particle-suspended methanol. *Chem. Eng. J.* **2006**, *119* (2), 107-112.
30. Andrews, E.; Ren, M.; Wang, F.; Zhang, Z.; Sprunger, P.; Kurtz, R.; Flake, J. Electrochemical Reduction of CO_2 at Cu Nanocluster / (100) ZnO Electrodes. *J. Electrochem. Soc.* **2013**, *160* (11), H841.
31. Rooney, C. L.; Lyons, M.; Wu, Y.; Hu, G.; Wang, M.; Choi, C.; Gao, Y.; Chang, C.-W.; Brudvig, G. W.; Feng, Z.; Wang, H. Active Sites of Cobalt Phthalocyanine in Electrocatalytic CO_2 Reduction to Methanol. *Angew. Chem. Int. Ed* **2024**, *63* (2), e202310623.
32. Zaupa, G.; Mora, C.; Bonomi, R.; Prins, L. J.; Scrimin, P. Catalytic Self-Assembled Monolayers on Au Nanoparticles: The Source of Catalysis of a Transphosphorylation Reaction. *Chem. Eur. J.* **2011**, *17* (17), 4879-4889.
33. Hara, K.; Akiyama, R.; Takakusagi, S.; Uosaki, K.; Yoshino, T.; Kagi, H.; Sawamura, M. Self-Assembled Monolayers of Compact Phosphanes with Alkanethiolate Pendant Groups: Remarkable Reusability and Substrate Selectivity in Rh Catalysis. *Angew. Chem. Int. Ed.* **2008**, *47* (30), 5627-5630.
34. Marshall, S. T.; Schwartz, D. K.; Medlin, J. W. Adsorption of Oxygenates on Alkanethiol-Functionalized Pd(111) Surfaces: Mechanistic Insights into the Role of Self-Assembled Monolayers on Catalysis. *Langmuir* **2011**, *27* (11), 6731-6737.
35. Novak, L. M.; Steyskal, E.-M. Electrochemical detection of fluoride ions in water with nanoporous gold modified by a boronic acid terminated self-assembled monolayer. *RSC Adv.* **2023**, *13* (10), 6947-6953.
36. Mandler, D.; Kraus-Ophir, S. Self-assembled monolayers (SAMs) for electrochemical sensing. *J. Solid State Electrochem.* **2011**, *15* (7), 1535-1558.
37. Guo, X.; Shi, Y.; Liu, P.; Ding, Y.; Du, B.; Liang, C.; Niu, W.; Tan, Y.; He, Y.; Chen, J.; et al. Dual Improvement in Sensitivity and Humidity Tolerance of a NO_2 Sensor Based on 3-Aminopropyltriethoxysilane Self-Assembled Monolayer-Functionalized SnSe2 for Explosive Photolysis Gas Detection. *ACS Appl. Mater. Int.* **2023**, *15* (23), 28358-28369.

38. Ramos, N. C.; Medlin, J. W.; Holewinski, A. Electrochemical Stability of Thiolate Self-Assembled Monolayers on Au, Pt, and Cu. *ACS Appl. Mater. Int.* **2023**, *15* (11), 14470-14480.
39. Peychev, B.; Slavchov, R. I. Interactions between Small Inorganic Ions and Uncharged Monolayers on the Water/Air Interface. *J. Phys. Chem. B* **2023**, *127* (12), 2801-2817.
40. Ensafi, A. A.; Alinajafi, H. A.; Jafari-Asl, M.; Rezaei, B. Self-assembled monolayer of 2-pyridinethiol@Pt-Au nanoparticles, a new electrocatalyst for reducing of CO_2 to methanol. *J. Electroanal. Chem.* **2017**, *804*, 29-35.
41. Tamura, J.; Ono, A.; Sugano, Y.; Huang, C.; Nishizawa, H.; Mikoshiba, S. Electrochemical reduction of CO_2 to ethylene glycol on imidazolium ion-terminated self-assembly monolayer-modified Au electrodes in an aqueous solution. *Phys. Chem. Chem. Phys.* **2015**, *17* (39), 26072-26078.
42. Yang, Z.; Wan, M.; Gu, Z.; Che, F. CO_2RR-to-CO Enhanced by Self-Assembled Monolayer and Ag Catalytic Interface. *J. Phys. Chem. C* **2023**, *127* (36), 17685-17693.
43. Mennel, J. A.; Pan, H.; Palladino, S. W.; Barile, C. J. Electrocatalytic CO_2 Reduction by Self-Assembled Monolayers of Metal Porphyrins. *J. Phys. Chem. C* **2020**, *124* (36), 19716-19724.
44. Pan, H.; Barile, C. J. Electrochemical CO_2 reduction to methane with remarkably high Faradaic efficiency in the presence of a proton permeable membrane. *Energy Environ. Sci.* **2020**, *13* (10), 3567-3578, 10.1039/D0EE02189J.
45. Akter, T.; Barile, C. J. Membrane-controlled CO_2 electrocatalysts with switchable C2 product selectivity and high faradaic efficiency for ethanol. *J. Mater. Chem. A* **2023**, *11* (21), 11354-11363, 10.1039/D3TA00613A.
46. Akter, T.; Pan, H.; Barile, C. J. Tandem Electrocatalytic CO_2 Reduction inside a Membrane with Enhanced Selectivity for Ethylene. *J. Phys. Chem. C* **2022**, *126* (24), 10045-10052.
47. Pan, H.; Akter, T.; Barile, C. J. Electrochemical CO_2 Reduction on Zinc and Brass with Modulated Proton Transfer Using Membrane-Modified Electrodes. *ACS Appl. Energy Mater.* **2022**, *5* (10), 12860-12868.

48. Pan, H.; Barile, C. J. Electrochemical CO_2 Reduction on Polycrystalline Copper by Modulating Proton Transfer with Fluoropolymer Composites. *ACS Appl. Energy Mater.* **2022**, *5* (4), 4712-4721.
49. Pan, H.; Barile, C. J. Titanium nitride-supported Cu–Ni bifunctional electrocatalysts for CO_2 reduction and the oxygen evolution reaction. *Sustain. Energy Fuels* **2020**, *4* (11), 5654-5664, 10.1039/D0SE01150A.
50. Pan, H.; Barile, C. J. Bifunctional nickel and copper electrocatalysts for CO_2 reduction and the oxygen evolution reaction. *J. Mater. Chem. A* **2020**, *8* (4), 1741-1748, 10.1039/C9TA12055F.
51. Okonkwo, P. C.; Ben Belgacem, I.; Emori, W.; Uzoma, P. C. Nafion degradation mechanisms in proton exchange membrane fuel cell (PEMFC) system: A review. *Int. J. Hydrog. Energy* **2021**, *46* (55), 27956-27973.
52. Kresse, G.; Hafner, J. Ab initio molecular dynamics for liquid metals. *Phys. Rev. B* **1993**, *47* (1), 558-561.
53. Kresse, G.; Furthmüller, J. Efficiency of ab-initio total energy calculations for metals and semiconductors using a plane-wave basis set. *Comput. Mater. Sci.* **1996**, *6* (1), 15-50.
54. Kresse, G.; Furthmüller, J. Efficient iterative schemes for ab initio total-energy calculations using a plane-wave basis set. *Phys. Rev. B* **1996**, *54* (16), 11169-11186.
55. Kresse, G.; Joubert, D. From ultrasoft pseudopotentials to the projector augmented-wave method. *Phys. Rev. B* **1999**, *59* (3), 1758-1775.
56. Perdew, J. P.; Burke, K.; Ernzerhof, M. Generalized Gradient Approximation Made Simple. *Phys. Rev. Lett.* **1996**, *77* (18), 3865-3868.
57. Grimme, S.; Ehrlich, S.; Goerigk, L. Effect of the damping function in dispersion corrected density functional theory. *J. Comput. Chem.* **2011**, *32* (7), 1456-1465.
58. Grimme, S.; Antony, J.; Ehrlich, S.; Krieg, H. A consistent and accurate ab initio parametrization of density functional dispersion correction (DFT-D) for the 94 elements H-Pu. *J. Chem. Phys.* **2010**, *132* (15), 154104.
59. Mathew, K.; Kolluru, V. S. C.; Mula, S.; Steinmann, S. N.; Hennig, R. G. Implicit self-consistent electrolyte model in plane-wave density-functional theory. *J. Chem. Phys* **2019**, *151* (23), 234101.

60. Mathew, K.; Sundararaman, R.; Letchworth-Weaver, K.; Arias, T. A.; Hennig, R. G. Implicit solvation model for density-functional study of nanocrystal surfaces and reaction pathways. *J. Chem. Phys.* **2014**, *140* (8), 084106.
61. Wang, V.; Xu, N.; Liu, J.-C.; Tang, G.; Geng, W.-T. VASPKIT: A user-friendly interface facilitating high-throughput computing and analysis using VASP code. *Comput. Phys. Commun.* **2021**, *267*, 108033.
62. Mondol, P.; Thind, J. K.; Barile, C. J. Selective Electrocatalytic Nitrate Reduction to Ammonia Using Nafion-Covered Cu Electrodeposits. *J. Phys. Chem. C* **2023**, *127* (17), 8054-8061.
63. Kim, M.; Schmitt, S. K.; Choi, J. W.; Krutty, J. D.; Gopalan, P. From Self-Assembled Monolayers to Coatings: Advances in the Synthesis and Nanobio Applications of Polymer Brushes. In *Polym.* **2015**, *7,* 1346-1378.
64. Luo, W.; Zhang, Q.; Zhang, J.; Moioli, E.; Zhao, K.; Züttel, A. Electrochemical reconstruction of ZnO for selective reduction of CO_2 to CO. *Appl. Catal. B: Environ.* **2020**, *273*, 119060.
65. Perkins, C. L. Molecular Anchors for Self-Assembled Monolayers on ZnO: A Direct Comparison of the Thiol and Phosphonic Acid Moieties. *J. Phys. Chem. C* **2009**, *113* (42), 18276-18286.
66. Rosen, J.; Hutchings, G. S.; Lu, Q.; Forest, R. V.; Moore, A.; Jiao, F. Electrodeposited Zn Dendrites with Enhanced CO Selectivity for Electrocatalytic CO_2 Reduction. *ACS Catal.* **2015**, *5* (8), 4586-4591.
67. Shayesteh, H.; Raji, F.; Kelishami, A. R. Influence of the alkyl chain length of surfactant on adsorption process: A case study. *Surf. Interfaces* **2021**, *22*, 100806.
68. Verma, C.; Quraishi, M. A.; Rhee, K. Y. Hydrophilicity and hydrophobicity consideration of organic surfactant compounds: Effect of alkyl chain length on corrosion protection. *Adv. Colloid Interface Sci.* **2022**, *306*, 102723.
69. Laviron, E. Adsorption, Autoinhibition and Autocatalysis in Polarography and in Linear Potential Sweep Voltammetry. *J. Electroanal. Chem.* **1974**, *52*, 355-393.
70. Clark, E. L.; Ringe, S.; Tang, M.; Walton, A.; Hahn, C.; Jaramillo, T. F.; Chan, K.; Bell, A. T. Influence of Atomic Surface Structure on the Activity of Ag for the Electrochemical Reduction of CO_2 to CO. *ACS Catal.* **2019**, *9* (5), 4006-4014.

TOC Graphic

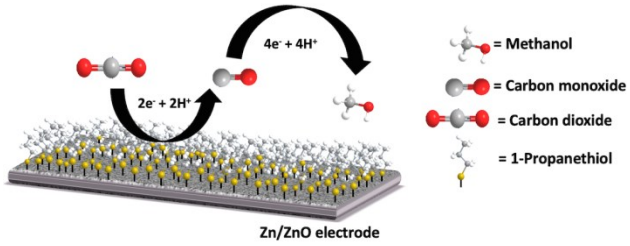
4e⁻ + 4H⁺
2e⁻ + 2H⁺
Zn/ZnO electrode
= Methanol
= Carbon monoxide
= Carbon dioxide
= 1-Propanethiol